García Sánchez, E.; Martínez Melero, M.; Úbeda Picot, MÁ.; Pérez Pla, F.; Marcos Martínez, MD.; El Haskouri, J.; Amorós, P. (2021). Nitroarene hydrogenation catalysts based on Pd nanoparticles glued with PDA on inorganic supports: Multivariate Curve Resolution as an useful tool to compare the catalytic activity in multi-step reactions. Applied Catalysis A General. 619:1-12. https://doi.org/10.1016/j.apcata.2021.118125

Nitroarene hydrogenation catalysts based on Pd nanoparticles glued with PDA on inorganic supports: Multivariate Curve Resolution as an useful tool to compare the catalytic activity in multi-step reactions

Elena García Sánchez[a], María Martínez Melero[b], M. Ángeles Úbeda Picot[a,*], Francisco Pérez Pla[a,*], M. Dolores Marcos[c], Jamal El Haskouri[a], Pedro Amorós[a,*]

[a]*Institut de Ciència dels Materials (ICMUV), Universitat de València, c/Catedrático José Beltrán 2, Paterna, 46980 València, Spain*
[b]*Departament de Química Inorgànica, Universitat de València, c/Dr. Moliner 50, Burjassot, 46100 Valencia, Spain*
[c]*Centro de Reconocimiento Molecular y Desarrollo Tecnológico (IDM), Unidad Mixta Universitat Politècnica de València-Universitat de València, Departamento de Química, Universitat Politècnica de València, Camino de Vera s/n, 46022 Valencia, Spain*

Abstract

Two green catalysts based on Pd(0) nanoparticles (Pd NPs) anchored through PDA on porous silica and magnetite have been synthesized using a generalized simple and reproducible "two-step" methodology. Both catalysts were tested for a model reaction, the hydrogenation of 4-nitrophenol using $NaBH_4$ as the hydrogenating agent, and especially good activity has been achieved in the case of the catalysts containing magnetite as inorganic core (Pd NPs-PDA@Fe_3O_4). We analyzed the effect associated with the catalyst separation method (centrifugation or magnetically) that affect to the distribution and aggregation degree of the Pd NPs. In addition, we also correlate the final catalyst morphology with the activity and its relationship with the nature of the inorganic supports: porous (UVM-7 type silica) or massive, although on a nanoscale, typical of the Fe_3O_4 particles used. We have also studied the activity of the catalysts in the hydrogenation of nitroarenes, that follows the Haber multistep mechanism through various intermediates. In order to understand not only the process as a whole, but also the importance of each step and the intermediates involved, we have applied the multivariate curve resolution (MCR) factorial methodology. This approach, that normally is not used in the catalysis works, makes it possible to quantitatively determine the rate limiting step, and allow to extract complete information from a multistep catalytic process.

Keywords:
mesoporous silica, magnetite, bimodal porosity, polydopamine, palladium, nanoparticles, 4-nitroarenes, multi-curve resolution factorial analysis

Email addresses: angeles.ubeda@uv.es (M. Ángeles Úbeda Picot), francisco.perez@uv.es (Francisco Pérez Pla), pedro.amoros@uv.es (Pedro Amorós)
[1]corresponding author

1. Introduction

The nitro aromatic compounds are widely used in the chemical industry for the manufacturing of pharmaceuticals, pesticides, dyes, pigments, explosives, plasticizers, and fungicides[1–5], being generated each year a large number of polluting waste hazardous for the environment. These anthropogenic, xenobiotic, and mutagenic/carcinogenic compounds are very toxic for human beings, animals, and plants[1, 5–9]. Of the group of nitroarenes, the nitrophenols are by-products in many industrial processes, and due to their solubility in water, they are usually found as refractory pollutants in wastewaters. In particular, 4-nitrophenol, an intermediate in the synthesis of paracetamol, is a chemical widely used [10]. As pollutant, it stays a longer time in water and soil without degradation and cause damage to the central nervous system, blood, kidney, and liver [5, 7, 11]. The United States Environmental Protection Agency (US-EPA) has declared the 4-nitrophenol and the other nitrophenols as priority pollutants, recommending low concentration (10.0 ng/mL) in water [2, 5, 8, 12–17]. The transformation of compounds of this nature into intermediates in the industrial productions is important for pollution remediation. The reduction of nitroarenes is one of the most used catalytic processes since the aniline and their derivatives represent a large part of the market in the organic chemical industry [17–23].

Nanoparticles (NPs) of noble metals (Au, Ag, Pd, Pt) or 3d-metals immobilized on inorganic, organic, or hybrid supports, have been applied in the catalytic reduction of nitroarenes [1, 2, 13, 18–20, 24–31]. The design of the morphology and organization of the catalysts in order to have more efficient active sites is of special relevance in the case of multicomponent catalysts, such as NPs incorporated on different supports. In the metal NPs immobilization, the control is lost in the interface, where the metal-support interaction plays a key role in the synthesis of an efficient catalyst [32, 33]. The modification of the support, aimed at generating a suitable environment that controls the charge and dispersion of the metal NPs, and avoiding their aggregation and leaching, is an interesting approach to the development of efficient metal NPs supported catalysts [34]. In this way of work, Lee and coworkers, inspired by the adhesive proteins in mussels, synthesized the polydopamine (PDA) from the low molecular weight biomolecule dopamine (DP) [34–36]. PDA, that exhibits strong adhesion on virtually any surface [37], has the ability to coordinate metal ions by their functional groups, and to reduce metal salts into metal NPs via the catechol groups [36, 37]. These characteristics can drive the interfacial assembly of metal NPs stabilizing them and avoiding the reduction of their activity, allowing the synthesis of more effective metal NPs supported catalysts. Metal NPs-PDA-supported materials have been synthesized and efficiently tested in some catalytic reactions [24, 38–52].

In a previous work, we synthesized a variety of Pd NPs-based catalysts anchored in a hybrid compound based on a porous silica (denoted UVM-7) combined with PDA (PDA@UVM-7) as a support that have proven to be very efficient for the reduction of hydrogenation of 4-nitrophenol [53]. The efficiency of these catalysts was superior to that of a similar material without PDA such as Pd NPs supported on UVM-7 silica [54]. That work allowed us to show the importance in the sequential order of incorporation of the different elements of the catalyst. The catalysts prepared using “two pot” strategies (first the formation of the PDA@UVM-7 support and the subsequent incorporation of Pd NPs) were more active than those synthesized by “one-pot” pathways (with simultaneous PDA polymerization and covering of the silica core, and formation of the Pd NPs).

Other transition metal oxides coated with PDA as interfacial glue have been used as inorganic supports to incorporate Pd NPs. In recent times, materials containing magnetite nanoparticles have seen their field of application extended in a great diversity of areas [55]. In catalysis, their use as support stands out since displayed a good magnetic separability and even reusability.

In the literature have been described some Pd NPs-PDA@Fe_3O_4 catalysts, in which magnetite cores have micrometric sizes and in some cases with spherical shapes [49, 56–65], or others that incorporate in the aforementioned material, silica [62], graphene [63], porous organic polymer (POP) [64], or MOFs [65]. These catalysts have been efficiently tested in the Suzuki-Miyaura [49, 57, 62] and Heck [59] cross-coupling reactions, bromate reduction by liquid phase catalytic hydrogenation [56], hydrolytic dehydrogenation of ammonia borane [58], oxidative dehydrogenation of benzyl alcohols [61], cyanation of haloarenes [63], nitroarene reductions by catalytic transfer hydrogenation (CTH) [59, 62, 65] or with H_2 [41, 60], and, also in the tandem cross-coupling nitroarene reductions [65].

At this point, it is worth noting that it should be possible to compare the activity of the different catalysts from the data reported in the literature. Nevertheless, most works report only yields and the value of the turn-over frequency (TOF), and only a few of them provide rate constants. Even in these cases, the values do not allow, sometimes, for easy comparison due to a non-uniformity in the criteria applied. Consequently, one of the basic objectives of this work was to develop comparison criteria for the activity applied to the reduction of nitroarenes.

The reduction by transfer hydrogenation of 4-nitrophenol is considered a "model catalytic reaction" [66], and has been accepted to test the activity of metal NPs catalysts [7, 24, 67]. Recently, our research group published a methodology based in the uncomplicated calculation of the values of $TOF_{1/2}$ (i.e. TOF calculated at the semi-reaction time) and the corrected TOF (i.e. $TOF_{1/2}/[BH_4^-]$) from the 4-nitrophenol reduction absorbance data [53] that can be used to compare the activity of any catalyst. The methodology was sufficient to establish comparisons between catalysts and different catalytic conditions. This method is a generalization of that developed by Larm et col. [68] for comparing the activity of Au NPs reported from various sources, as it does not assume that the catalytic reduction of 4-nitrophenol is always a first-order process.

However, sometimes, the use of the model reaction is not enough for a complete understanding of the catalytic process, especially when it is of multi-step nature. So, more powerful analysis methodologies are necessary to be implemented. This is the case when we try to understand the reduction of other pollutants nitroarenes, in which intermediates of the Haber mechanism are observed [69, 70]. For these systems, we have applied the multivariate curve resolution (MCR) factorial methodology of absorbance data [71–73]. MCR has been commonly used in analytical chemistry and engineering but, to our knowledge, this is the first time it has been applied to extract complete information from a catalytic process. The method makes it possible to quantitatively determine the rate limiting step, and the relative catalyst activity of each reduction process. This methodology could be generalized for other multi-step reactions, and it would be interesting to adjust the reaction conditions to improve the final yields. In this way, the application of the MCR methodology constitutes an additional tool that complements the sophisticated characterization techniques used for the study of catalysts (before, during and after their use) to understand multi-step heterogeneous phase catalytic processes. In addition, the information obtained through this methodology is direct, and it refers to the catalytic system considered as a whole (substrate, catalyst, conditions…).

In summary, we extend in this paper our simple "two-step" catalysts preparative method by anchoring Pd NP through PDA to alternative inorganic supports other than silica, such as magnetite NPs. This methodology can be extended to immobilize metallic NPs on any organic or inorganic support. The simplest magnetite/PDA/Pd based catalyst has been prepared and thoroughly characterized. The activity of both catalysts (with silica core (UVM-7) and magnetite) has been compared for the hydrogenation of 4-nitrophenol. The use of the MCR factorial method-

ology in catalytic applications is presented for the first time for the understanding of multi-step processes involving the hydrogenation of other nitroarenes,

2. Experimental

2.1. Reagents and materials

The mesoporous silica UVM-7 was synthesized according to the procedure described in the literature [74]. Commercially available methanol (MeOH), HCl, KCl, dopamine hydrochloride (DA), $PdCl_2$, 4-substituted nitrobenzene compounds, and $NaBH_4$ were supplied by Aldrich. HPLC grade CH_3CN (from Baker). All reagents were used without further purification.

2.2. Preparation of Pd NPs-PDA@UVM-7 catalyst

The synthesis of this catalyst was previously described in detail through a two-step procedure starting from a bimodal porous silica denoted as UVM-7 as inorganic support. The first stage corresponds to the formation of the PDA coating on the silica surface. Later, PDA@UVM-7 (650 mg) was dispersed in H_2O (50 mL). A solution of $H_2[PdCl_4]$ obtained by reaction of $PdCl_2$ (37 mg, 0.21 mmol) with HCl (0.2 M, 2.1 mL) was added, and the suspension was stirred for 24 h. The resulting solid was dispersed in H_2O (50 mL), and 10 mL of a freshly solution of $NaBH_4$ (0.07 M) was added slowly. The dispersion was sonicated during 1 h and kept under stirring for 24 h. The solid was washed by centrifugation only once with $EtOH/H_2O$ (1:1 v/v) and air dried.

2.3. Preparation of Pd NPs-PDA@Fe_3O_4 catalyst.

2.3.1. Synthesis of Fe_3O_4

In a three-necked flask and under nitrogen atmosphere, $FeCl_2 \cdot 4\ H_2O$ (3.023 g, 15.2 mmol) and $FeCl_3 \cdot 6\ H_2O$ (6.123 g, 22.7 mmol) were dissolved in H_2O (20 mL). The solution was heated to 80 ºC and a solution of H_2O:NH_3 (1:3, 35% in ammonia, 20 mL) was added using a perfusion pump (0.5 mL/min). The obtained suspension was kept at 100ºC under stirring for two hours. After this time, the suspension was cooled at room temperature and the solid, Fe_3O_4, was separated using a neodymium magnet. The solid was washed with water and methanol, and dried at 75 ºC for 24 hours (2.301 g).

2.3.2. Coating the Fe_3O_4 with polydopamine (PDA@Fe_3O_4)

Fe_3O_4 (596 mg, 2.6 mmol) was dispersed in a tris(hydroxymethyl) aminomethane hydrochloride buffer (Tris-HCl, 10 mM, pH = 8.5, 60 mL) and the suspension was sonicated during 45 min. After that, DA (209 mg, 1.4 mmol) was added. The suspension was again sonicated during other 45 min and kept under stirring for 24 h. The dark brown solid obtained was magnetically separated and washed, first with H_2O and finally with $MeOH/H_2O$ (1:1 v/v) until to get a colorless wash water. The solid was dried at 60 ºC (615 mg).

2.3.3. Immobilization of Pd NPs on PDA@Fe_3O_4

PDA@Fe_3O_4 (500 mg) was dispersed in H_2O (50 mL) that contained sodium dodecyl sulfate (NaSDS). The suspension was sonicated during 30 min and an aqueous solution of $H_2[PdCl_4]$ (5 mL), prepared dissolving $PdCl_2$ (19 mg, 0.11 mmol) with HCl (0.1 M, 2.1 mL), was added using a perfusion pump (0.5 mL/min). The suspension was sonicated during other 30 min and kept under stirring for 24 h. The solid magnetically isolated, was dispersed in H_2O (50 mL) and sonicated for 15 min after which, and under stirring, 10 mL of a freshly solution of $NaBH_4$ (0.07 M) was added using a perfusion pump (0.5 mL/min). The solid was washed with H_2O and MeOH and dried at 60ºC (471 mg).

2.4. Characterization techniques

TGA (Thermal Gravimetric Analysis) curves were recorded with a Setaram Setsys 16/18 thermobalance (Setaram Instrumentation, Caluire-et-Cuire, France) under an air atmosphere flowing at 25 ml per min (heating rate of 5 ºC/min).

The Pd contents were determined by energy dispersive X-ray spectroscopy (EDX) analysis using a scanning electron microscope (Philips-SEM-XL 30 (Eindhoven, The Netherlands). For electron microscopy analyses, the samples were dispersed in ethanol and placed onto a carbon coated copper microgrid and left to dry before observation.

The TEM (transmission electron microscopy) and HRTEM (high resolution transmission electron microscopy) microstructural characterizations were carried out using a JEOL JEM-1010 instrument operating at 100 kV and equipped with a CCD camera and a Tecnai G2 F20(FI) instrument, respectively.

STEM-HAADF (scanning transmission electron microscopy-high-angle annular dark-field) images were acquired on a JEOL-2100F microscope operated at 200 kV (JEOL Ltd., Tokio, Japan).

Powder X-ray diffraction (XRD) was carried out using a Bruker D8 Advance diffractometer (Bruker AXS GmbH, Karlsruhe, Germany) with monochromatic Cu Kα source operated at 40 kV and 40 mA. Patterns were collected in steps of 0.02º (2θ) over the angular range 1-10º (2θ),
with an acquisition time of 25 s per step. Additionally, XRD patterns were recorded over a wider angular range, 10–80 º(2θ) to determine the presence of segregated crystalline phases.

X-ray photoelectron spectroscopy (XPS) measurements were carried out on a K-Alpha X ray Photoelectron Spectrometer System using a monochromatic Al K(α) source (1486.6 eV). The C 1s peak (284.6 eV) was used for the calibration of the binding energy.

Surface area values were calculated from nitrogen adsorption-desorption isotherms recorded in an automated Micromeritics ASAP2020 instrument (Micromeritics Instrument Corp., Norcross, GA, USA). Prior to the adsorption measurements, the samples were out-gassed in situ in vacuum (10^{-6} Torr) at 120 ºC for 15 hours to remove adsorbed gases. Surface areas were estimated according to the Brunauer-Emmett-Teller (BET) model , and pore size dimensions and pore volumes were calculated by using the Barrett-Joyner-Halenda (BJH) [75], and the nonlocal density functional theory (NLDFT) methods [76].

2.5. Kinetic experiments

Stock solutions of Pd NPs-PDA@Fe_3O_4 and Pd NPs-PDA7@UVM-7 catalysts were prepared dispersing by sonication the appropriate mass of the material (4-5 mg) in low conductivity water (5 mL, [Pd] $\approx 2.2 \times 10^{-4}$ M). Reaction mixtures were prepared by mixing a stock solution of the nitroarene (1.5 ml, 0.7 – 1.4 $\times 10^{-4}$ M), low-conductivity water (1.5 mL), $NaBH_4$ (5 mg, 4.4×10^{-2} M), and the stock solution of the catalyst (5 μL, [Pd] $\approx 3.6 \times 10^{-7}$ M) in a quartz-cell (path-length 1 cm). For 4-nitrophenol, solutions were prepared according to the procedure described, but using water as the solvent.

The progress of nitroarene reduction was monitored using a diode-array UV/Vis Agilent 8453 spectrophotometer. In order to record the absorbance, the instrument was zeroed against a solution of MeOH:water (1:1 v/v, only H_2O in case of 4-nitrophenol). Thereafter, the spectrum of a solution containing $NaBH_4$ and a catalyst dispersion having the same concentration as the reaction mixture was recorded. The absorbance spectra were corrected by subtracting the catalyst/$NaBH_4$ spectrum. The reaction mixture was stirred to prevent catalyst deposition and hydrogen bubbles fixing on the cell walls.

2.6. Data analysis

2.6.1. Calculation of the turn-over frequency (TOF)

With the aim to compare the catalytic activity, the remaining fraction of the limiting reagent ($x(t)$) was calculated using Eq. 1,

$$x(t) = \frac{[NO_2C_6H_4R]}{[NO_2C_6H_4R]_0} = \frac{A_t - A_\infty}{A_0 - A_\infty} \qquad (1)$$

where A_t is the absorbance at time t at 400 nm (4-nitrophenolate anion maximum absorbance), A_0 is the absorbance at $t = 0$, and A_∞ stands for this magnitude at infinity time. After interpolating the reaction half-time ($t_{1/2}$) on the $x(t)$ graph (Fig. 6, vide infra), the average turn over frequency was estimated using Eq. 2,

$$TOF_{1/2} = TOF\left(t_{\frac{1}{2}}\right) = \frac{1}{2}\frac{[NO_2C_6H_4R]_{t=0}}{t_{1/2}\,[Pd]} \qquad (2)$$

where [Pd] is the Pd concentration in the reactor. Finally, in order to compare experiments carried out with different amounts of the co-reactant ($NaBH_4$), a corrected TOF was defined as $TOF_{1/2}/[NaBH_4]$.

2.6.2. Description of MCR method

In modern kinetic experiments, a physical property, v.g. the absorbance, is monitored along time through several observation channels leading to responses structured in two dimensions. A typical technique providing two-dimensional data is, for instance, diode-array (DA)UV-vis spectrophotometry. In this technique, the absorbance of reactive mixtures (**A**) is expressed as the product of matrices **C** and **S**, in accordance to the Lambert-Beer law,

$$\mathbf{A}(n_t, n_r) = \mathbf{C}(n_t, n_s)\mathbf{S}(n_s, n_r) + \mathbf{E}(n_t, n_r) \qquad (3)$$

In Eq. 3 n_t and n_r stand for the number of measurements and observation channels (wavelengths), $\mathbf{C}(n_t \times n_s)$ stores the concentration-time profiles for the n_s species considered, $\mathbf{S}(n_s \times n_r)$ contains the optical density spectra, and **E** is experimental uncertainty array. As usual, the difference between experimental absorbance and that calculated from the model was arranged in the matrix of residuals (**R**) defined by Eq. (4),

$$\mathbf{R}(\mathbf{a}, \mathbf{S}) = \mathbf{A} - \mathbf{CS} \qquad (4)$$

Minimization of residuals by means of multivariate curve resolution (MCR) methods enables the model validity to be checked . Usually, the large amount of responses provided by diode-array detector (512 observation channels in ours experiments) make the number of linear parameters (**S**) excessively large to a proper a classical non-linear optimization. MCR applies two complementary approaches to solve this issue, namely the factorization of the response matrix [77–80] and the effective elimination from Eq.(4) of the linear parameters [81, 82]. Factorization is achieved by means of singular value decomposition (SVD) of the response array ($\mathbf{A} = \mathbf{U}\Lambda\mathbf{V}^T$), where array $\mathbf{U}(n_t \times n_f)$ provides the abstract concentrations associated to the n_f significant factors, the diagonal array $\Lambda(n_f \times n_f)$ contains the singular values, and $\mathbf{V}(n_f \times n_s)$ accounts for the n_f representative abstract spectra (i.e. those not associated to null singular values). The reduction in size is achieved multiplying both sides of Eq. (4) by **V**,

$$\mathbf{R}_u = \mathbf{RV} = \mathbf{XV} - \mathbf{CSV} = \mathbf{X}_u - \mathbf{CS}_u \qquad (5)$$

As previously stated, optimization was greatly simplified when linear parameters were eliminated from Eq. (5). This was carried out by replacing them by their least-square estimations, $\mathbf{S}_u = \mathbf{C}^+\mathbf{X}_u$ ($\mathbf{C}^+ = (\mathbf{C}^T\mathbf{C})^{-1}\mathbf{C}^T$). This operation converts the residuals into a function depending only on kinetic **a** parameters (through **C**(**a**) array),

$$\mathbf{R}_u(\mathbf{a}) = (\mathbf{I} - \mathbf{C}\mathbf{C}^+)\mathbf{X}_u \quad (6)$$

where **I** was de identity matrix. Finally, a_i parameters were estimated form the non-linear regression of Eq.7, where (tr) stands for the matrix trace operator.

$$\phi(\mathbf{a}) = \mathrm{tr}(\mathbf{R}_u\mathbf{R}_u^T) \quad (7)$$

Calculations were performed with an ad hoc software (OPKMCR) developed in our laboratory written in the Julia programming language [83]. Minimization of Eq. 7 was carried out using the Nelder-Mead method [84] implemented in the NLOPT library [85], and integration of the stiff ODE in Eq. 14 (vide infra) was performed using a Gear like method [86] implemented in the DifferentialEquations Julia's package [87].

3. Results and discussion

3.1. Synthesis strategy

Pd NPs-PDA@UVM-7 and Pd NPs-PDA@Fe_3O_4 materials were prepared following the best strategy described in a previous study [53]. This strategy corresponds to a "two-pot" methodology in which, in a first step, the support (mesoporous silica (UVM-7) or Fe_3O_4 NPs) was coated with PDA through polymerization of DA in a buffered medium. The second step consisted of the Pd(II) incorporation using $H_2[PdCl_4]$ as the metal source. After removal of Pd(II) excess not immobilized on the support, the reduction with $NaBH_4$ resulted in the formation of Pd NPs (Figure 1). This strategy gave better results than those of the "one-pot" type, in which the PDA polymerization and the incorporation of palladium was carried out simultaneously. As expected, "one-pot" type strategies favored the Pd NPs trapping, the final materials being richer in Pd, but their catalytic activity was impaired by the difficulty of the substrates to access the active centers (totally or partially covered with PDA). Therefore, regardless of the inorganic support used (silica or magnetite), we have opted for the "two-pot" strategy.

In our previous work on Pd NPs-PDA@UVM-7 catalysts, we observed that the leaching of Pd with the washings gave rise to very active materials, but very poor in Pd NPs and with a certain heterogeneity in terms of their dispersion. Therefore, and also with the aim of having two catalysts with a similar Si/Pd and Fe/Pd molar ratios for comparative purposes, we slightly modified our original preparative protocol by performing only a final washing step.

3.2. Catalysts characterization

The final averaged stoichiometry of the materials was obtained by combining the TGA and EDX data. Both TGA curves (Figure S1) show an initial low temperature weight loss (up to ca. 100 ºC) that can only be attributed to water molecules. This first weight loss is significantly more pronounced in the case of the catalyst built on the porous silica support. The open architecture and large surface area of UVM-7 silica can retain a higher proportion of water molecules than massive Fe_3O_4 nanoparticles, due to its non-porous outer surface. PDA pyrolysis occurs in the temperature range of ca. 100-800 ºC. Based on the TGA data, we estimate a PDA amount

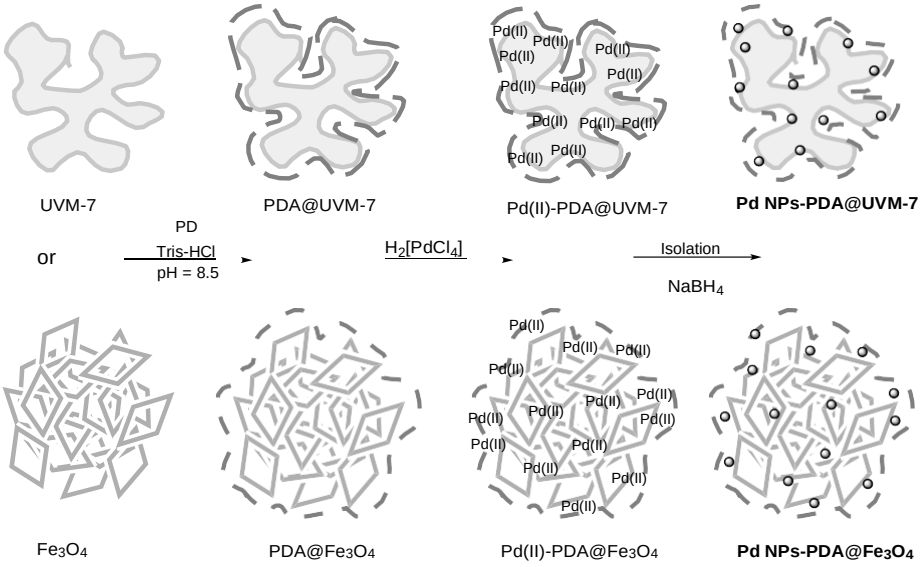

Figure 1: Scheme showing the strategy in the synthesis of both catalysts, Pd NPs-PDA@UVM-7 and Pd NPs-PDA@Fe_3O_4

similar for both catalysts. On the other hand, we have used EDX to assess both the stoichiometry and the chemical homogeneity of the catalysts, given that an important objective of our work is to favor also a good dispersion of Pd. The real Si/Pd and Fe/Pd molar ratios are 38 and 51, respectively. Thus, the modification of the synthesis procedure for the Pd NPs-PDA@UVM-7 catalyst carried out in the washing stage has allowed us to remarkably increase the amount of Pd (from Si/Pd = 768 in our previous work to Si/Pd = 38), also improving the dispersion of Pd NPs (see below). EDX data show that all the reported materials are chemically homogeneous at the spot area scale (ca. 1μm). In conclusion, the achieved catalysts formulations are as follows: $[(SiO_2)_{38}\ Pd]_{0.75}(PDA)_{0.11}(H_2O)_{0.14}$ and $[(Fe_3O_4)_{17}Pd]_{0.87}\ (PDA)_{0.12}(H_2O)_{0.02}$.

Once the catalysts stoichiometry has been determined, we will analyze their organization at the nano-scale combining HRTEM, HAADF, STEM-mapping, XRD and adsorption desorption N_2 isotherms. TEM and HRTEM images of the palladium-rich Pd NPs-PDA@UVM-7 catalyst are shown in Figure 2. According to our previous work, the typical open architecture of the UVM-7 silica support is preserved (Figure 2a). The higher palladium content compared to our previous work is clearly evident when looking at the STEM-HAADF image (Figure 2b). The Pd NPs distribution in the Pd NPs-UVM-7@PDA catalyst shows a higher homogeneity and the size of some bright spots is significantly larger (up to ca. 30-40 nm). The STEM-mapping (Figure S2) shows homogeneous distributions at the nano-scale of Si (from the UVM-7 silica), N and C (from the PDA) and Pd. The HRTEM images (Figure 2c and d) of the Pd NPs-PDA@UVM-7 catalyst clearly display the presence of ordered nanodomains which correspond to the Pd NPs. A combination of small aggregates (in the 4-7 nm range; Figure 2c) of Pd NPs is observed along with larger clusters (30-40 nm; Figure 2d) according to the STEM-HAADF images. In any case, it is important to remark that both the small and the large clusters are formed by aggregation of very small Pd NPs with homogeneous sizes around 2-3 nm. The small size of the Pd individual crystallites precludes its detection by diffraction techniques. In fact, no diffraction peaks are

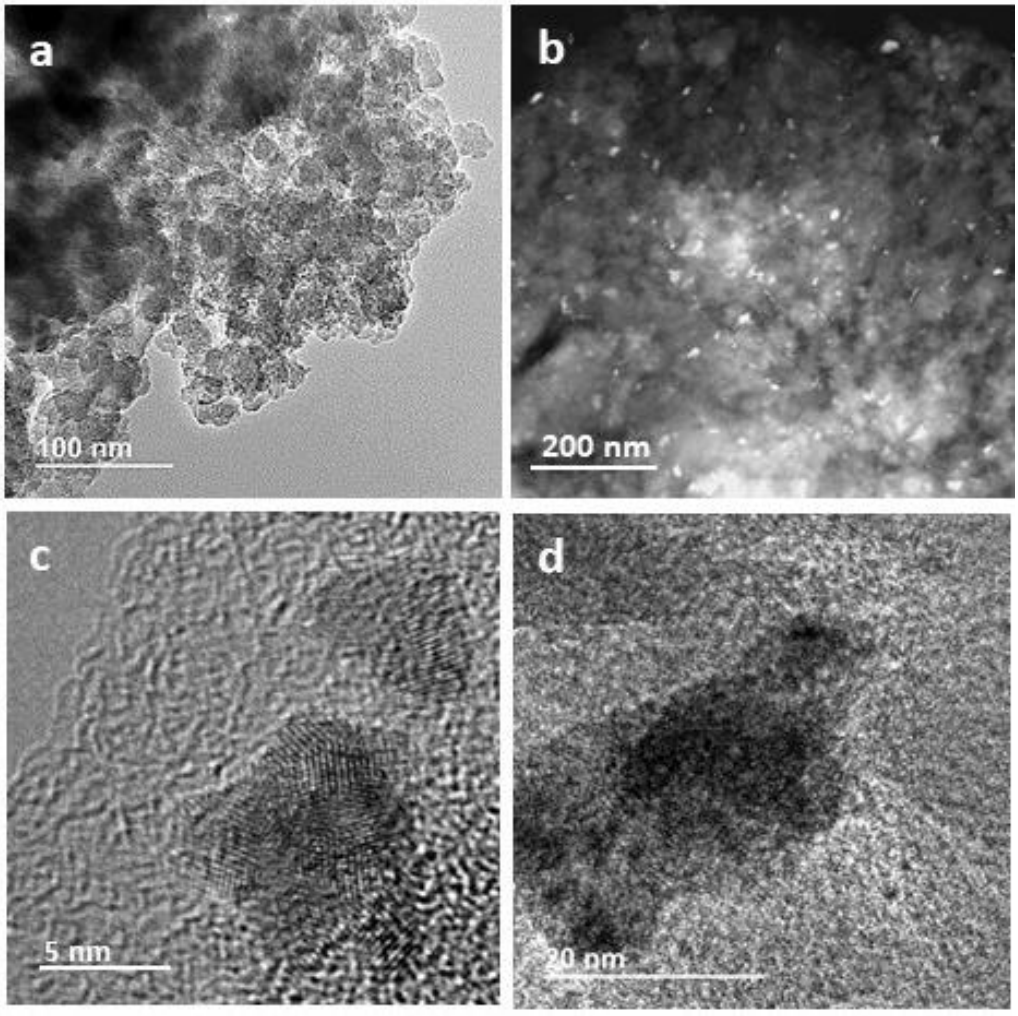

Figure 2: Electron microscopy images of the Pd NPs-PDA@UVM-7 catalyst. (a) Low magnification TEM image showing the preservation of the UVM-7 silica architecture. (b) HAADF-STEM image showing the Pd dispersion. HRTEM images showing the presence of small (c) and large (d) aggregates of Pd NPs.

recorded in the high-angle domain of the XRD pattern.

The bimodal hierarchical porosity typical of the UVM-7 silica-based support is preserved in a large extent after incorporation of the PDA and Pd according to the N_2 adsorption-desorption isotherm (Figure S3): two well defined adsorption steps can be observed at medium (P/P_0 < 0.3 – 0.5 < P/P_0) and high (P/P_0 > 0.8) relative pressure values that are associated with the intraparticle mesopores and the large interparticle voids, respectively. The catalyst has a high surface BET area of 622 m^2/g.

TEM and HRTEM images of the Pd NPs-PDA@Fe_3O_4 catalyst are shown in Figure 3. As expected, its morphology consists in aggregates of magnetite nanoparticles joined by the PDA.

To some extent, the image with lower magnification (Figure 3a) has certain similarities with that of the silica catalyst (inset in Figure 3a). The ordered domains correspond to the magnetite

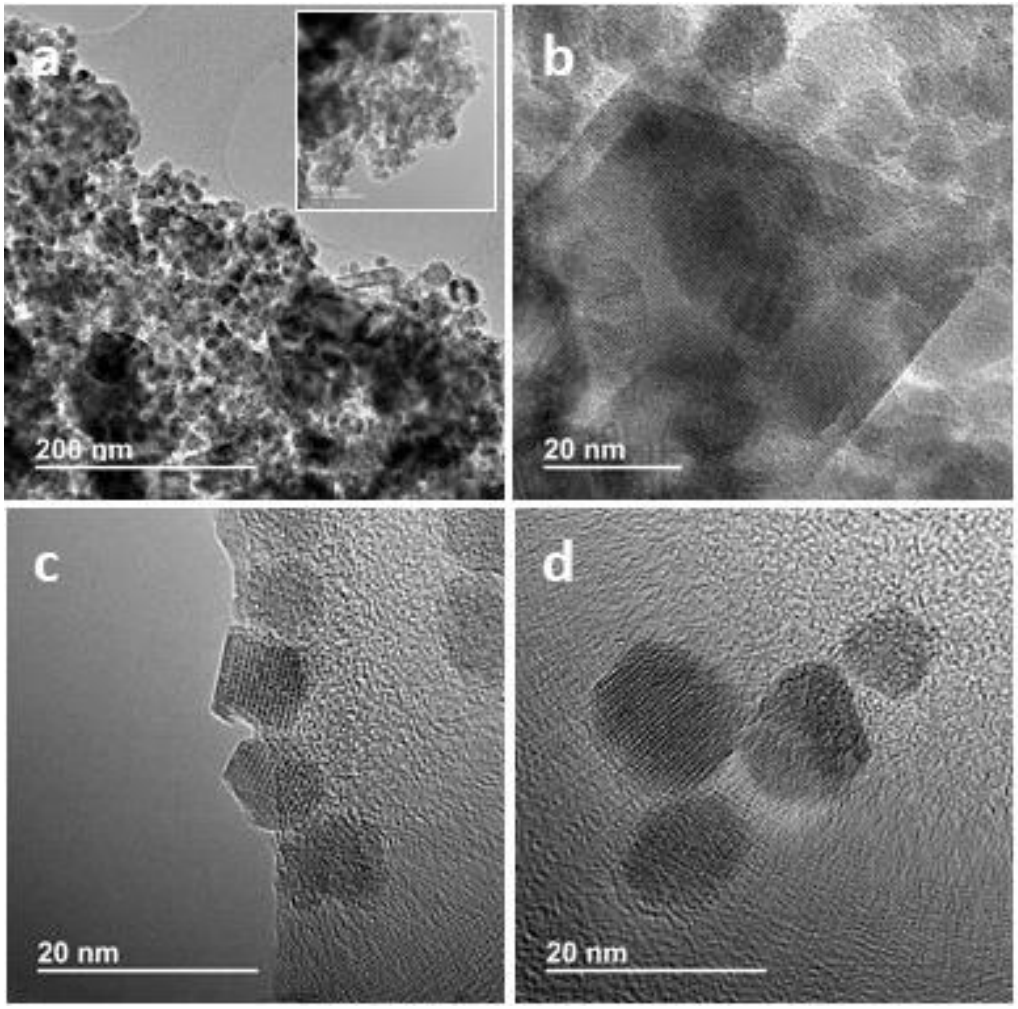

Figure 3: TEM images of the Pd NPs-PDA@Fe_3O_4 catalyst. (a) Low magnification TEM image showing the role played by PDA favoring the nanoparticle aggregation. (b) (c) and (d) HRTEM images show the coexistence of small and large Fe_3O_4 particles (b), partially (c) or completely embedded (d) in the PDA.

particles (Figures 3b, 3c and 3d), while the disordered areas must be associated to the amorphous PDA. The Fe_3O_4 nanoparticles show certain size heterogeneity. The mean size of the majority particles is in the range 10-20 nm (Figures 3c and 3d), which coexist with larger particles (Figure 3a and 3b). Both the small and large magnetite particles show well defined facets and planes due to its crystalline nature. This is in contrast to the images of the Pd NPs-PDA@UVM-7 catalyst in which the amorphous nature of the UVM-7 nanoparticles results in pseudo spherical and poorly defined geometries. On the other hand, the lower contrast in STEM-HAADF images between the magnetite and palladium domains when compared to the silica-based catalyst makes

it difficult to determine the size of the Pd NPs. The STEM-HAADF image (Figure 4) shows

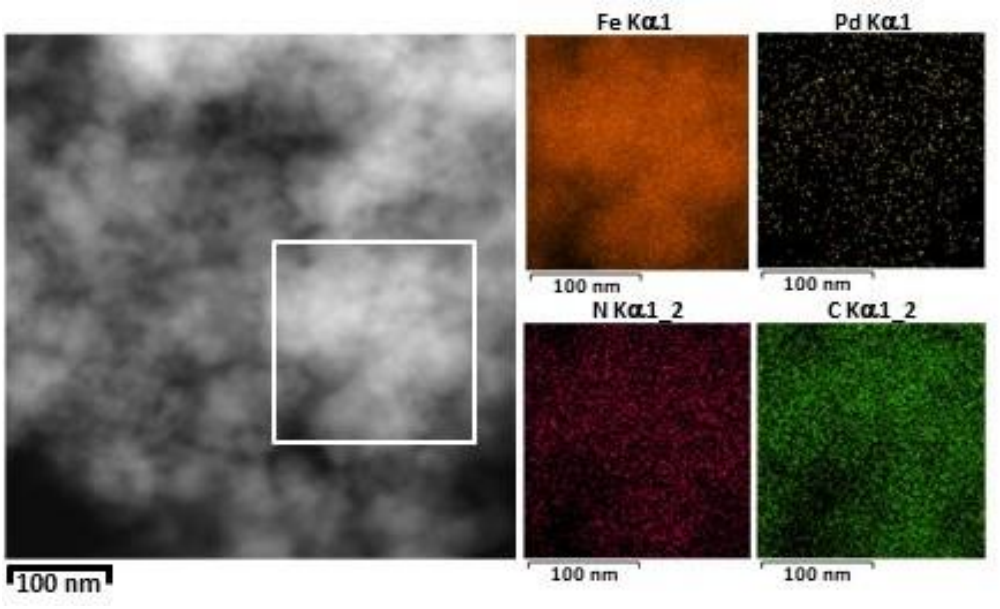

Figure 4: HAADF-STEM image of the Pd NPs-PDA@Fe_3O_4 catalyst including an EDX mapping of the selected area showing the Fe, Pd, N and C distribution.

the absence of bright spots associated to Pd NPs. An homogeneous and continuous bright is observed throughout the entire mass of the catalyst. In addition, the dispersion of Fe, Pd, N and C has been studied by spherical aberration (Cs) corrected STEM-HAADF. The mappings of the selected elements are included in Figure 4. Pd-rich zones are not detected. There is a regular and homogeneous distribution of all catalyst components (magnetite, palladium and PDA). Most likely, some ordered nano-domains seen in HRTEM images could correspond to Pd NPs. Furthermore, it must be taken into account that when the catalyst is separated by the action of a magnetic field (and not by centrifugation) only the Pd NPs stuck to the PDA will be retained. This could prevent some aggregation as occurs when separating the material by centrifugation. Thus, the aggregates of Pd NPs must have on average dimensions smaller than those observed for the catalyst with silica support.

The XRD pattern of the Pd NPs-PDA@Fe_3O_4 catalyst is shown in Figure 5. We can unequivocally confirm the presence of the diffraction peaks associated with magnetite, as well as the absence of signals attributable to Pd crystals. The relatively large *fwhm* value of the magnetite peaks is indicative of their nanometric nature. Applying the Scherrer equation, a mean crystallite size of ca. 14 nm has been determined, in good agreement with HRTEM images. In any case, the average size of thos magnetite particles is sognificantly smaller tha that described for other material/catalysts. It is far from the classical limit of 100 nm and so we can clearly establish that our magnetic core is made up of magnetite NPs. On the other hand, and as we discussed previously for the silica catalyst, the complete absence of XRD signals associated with palladium crystals suggests that their maximum size should be less than 5 nm.

An XPS analysis was carried out to determine the oxidation state od Pd. The XPS spectrum

(Figure S4) shows the presence of Pd(0) and Pd(II). The peaks at 335.7 and 340.9 eV are related to the core lines of Pd 3 $d_{3/2}$ and Pd 3 $d_{5/2}$ of Pd(0) (Pd NPs), respectively. Furthermore, the deconvolution of spectrum allows the identification of two additional signals at 338.0 (Pd 3 $d_{3/2}$) and 343.4 eV (3 $d_{5/2}$) typical of Pd(II) species. The Pd(0) NPs are the dominant species since the ratio Pd(II)/Pd(0)= 0.6.

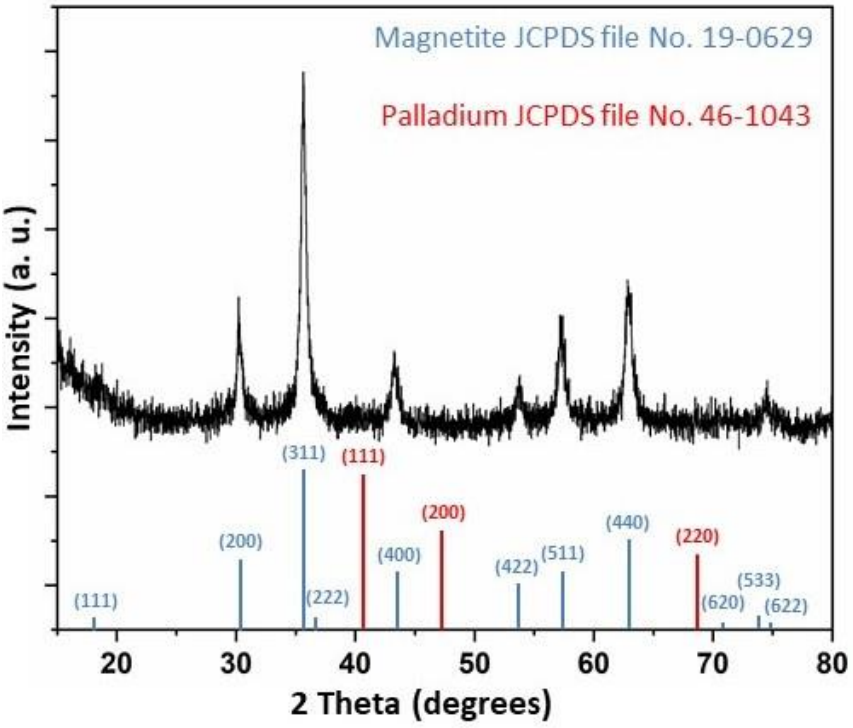

Figure 5: XRD pattern of the Pd NPs-PDA@Fe_3O_4 catalyst.

Although the support of the Pd NPs-PDA@Fe_3O_4 catalyst is not porous, the nanometric size of the magnetite particles and their subsequent coating with PDA (in a low proportion with respect to the inorganic component) allows the formation of a nanocomposite with some meso-porosity. As shown in Figure S4, its N_2 adsorption-desorption isotherm shows a single adsorption step at a high relative pressure value ($P/P_0 > 0.8$). The Pd NPs-PDA@Fe_3O_4 catalyst has a BET area of 57 m^2/g with volume and pore size values of 0.21 cm^3/g and 15.4 nm (determined through the application of the BJH model), and 0.14 cm^3/g and 18.3 nm (determined using the NLDFT model) respectively. This textural type porosity will favor the access of organic substrates to the active centers (Pd NPs) isolated and glued on the PDA surface.

Although the catalysts formulation presents similarities regarding the Si/Pd and Fe/Pd relative contents, as well as in the final PDA amount, their differences in morphology are quite marked. From an applied point of view, to dispose of an inorganic core with (Fe_3O_4) or without (SiO_2) magnetic activity allows the use of different separation strategies, and this can affect the aggregation/dispersion of the Pd NPs. The centrifugation process used to isolate the Pd NPs-

Table 1: Turnover frequencies for catalysts Pd NPs-PDA@Fe_3O_4 and Pd NPs-PDA@UVM-7 calculated from absorbance at 405 nm at room temperature in water.

support	[NP]	[Pd]	[$NaBH_4$]	$t_{1/2}$	†$TOF_{1/2}$	††$TOF_{1/2c}$
	$\times 10^5$/M	/ $\times 10^7$M	/ $\times 10^2$M	/s	$\times 10^{-3}/h^{-1}$	$\times 10^{-4}/h^{-1}M^{-}$
PDA@Fe_3O_4	7.0	3.6	4.66	109	3.15	7:5
PDA@UVM-7	7.4	5.9	4.49	127	1.76	3.9

† $TOF_{1/2} = \frac{1}{2}[NO_2C_6H_4OH]_0/(t_{1/2}[Pd])$; †† $TOF_{1/2c} = TOF_{1/2}/[NaBH_4]$.

PDA@UVM-7 catalyst favors the aggregation of the Pd NPs. Therefore, larger domains formed by Pd NPs are observed when compared to the Pd NPs-PDA@Fe_3O_4 catalyst.

Given that the active centers are the Pd NPs, and these are separated from the inorganic core by the PDA polymer, it can be assumed that the chemical nature of the inorganic core will not have great importance on the catalytic activity. More relevance may have the final morphology of the catalyst. In the case of Pd NPs-PDA@UVM-7, the typical hierarchical porosity of UVM-7 silica is preserved to some extent. This implies that the active Pd NPs will be distributed along a meso-macroporous network, which implies a certain confinement degree. This can affect reagent and product diffusion processes (although in all cases the substrates used are significantly smaller than the existing pores). On the contrary, the final morphology of the Pd NPs-PDA@Fe_3O_4 catalyst does not seem to be so influenced by the size and shape of the magnetite particles, but rather by the coverage that is generated when polymerizing the PDA around them. However, the combination of nano-sized magnetite particles and relatively low amount of PDA make it possible to achieve BET area values higher than those obtained from magnetic microparticles and higher values of polymeric coating. Then, even thought the Pd NPs-PDA@Fe_3O_4 catalyst has not intrinsic pores (like the Pd NPs-PDA@UVM-7), it shows a certain porosity (according to the N_2 adsorption-desorption isotherms) of a textural type associated to the voids amount PDA@Fe_3O_4 aggregates. In this case, the Pd NPs, in addition to being smaller and more dispersed aggregates (thanks to magnetic separation), they are not housed in such confined spaces, but preferably on the outer surface of the catalyst grains. Both TEM, XRD and porosimetry data are in good agreement with the exposed differences.

3.3. Catalyst activity

3.3.1. Catalyst activity with regard 4-nitrophenol

The catalytic activity of materials was compared using the hydrogenation of 4-nitrophenol with $NaBH_4$ as the reference model, which formally occurs as shown in Eq. 8,

$$NO_2-C_6H_4-OH + 2\,H_2 \xrightarrow{Pd,\ H_2O} NH_2-C_6H_4-OH + 2\,H_2O \qquad (8)$$

With the aim to compare the activity of materials, the turn-over frequency at the semi-reaction time ($TOF_{1/2}$) was estimated using Eq. 2 according to a previously published methodology [53] (Figures 6, S5). Results are presented in Table 1.

The $TOF_{1/2}$ value (1760 h^{-1}) of Pd NPs-PDA@UVM-7 (1) was similar to that reported for other Pd NPs supported on PDA@UVM-7 [53]. Nevertheless, the material was less active than the catalyst prepared using the best strategy in that work ($TOF_{1/2}$ = 8470 h^{-1}). The fact that

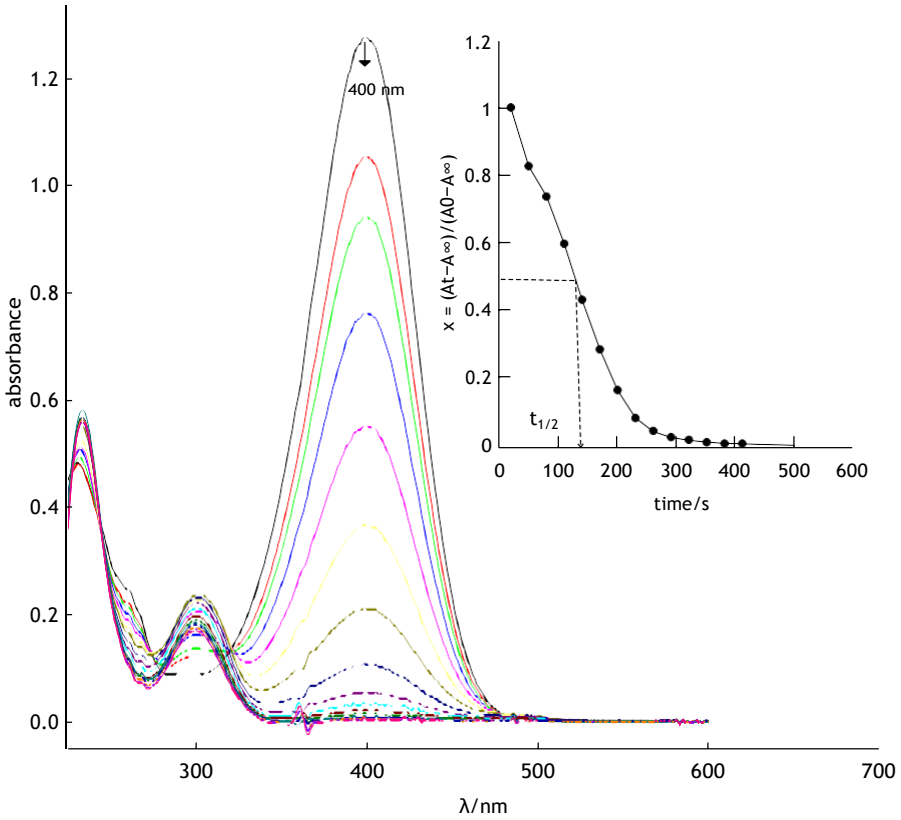

Figure 6: Variation of absorbance for the reduction of 4-nitrophenolate with $NaBH_4$ catalyzed by Pd NPs-PDA@Fe_3O_4; initial conditions are given in Table 1.**Inset**: Determination of $t_{1/2}$ used for calculation of $TOF_{1/2}$; Conversion ($x(t) = (A_t - A_\infty)/(A_0 - A_\infty)$) was calculated from the absorbance at 405 nm (max. optical density of 4-nitrophenolate).

the number of washing cycles has been decreased in the actual synthesis leads to a catalyst with higher Pd load (Si/Pd = 768 [53], Si/Pd = 38 this work), but having the Pd crystallites highly aggregated. Probably, this causes a significant part of the Pd in the larger aggregates to be unavailable for catalysis, decreasing then the activity per mole of palladium.

The comparison of $TOF_{1/2}$ values of materials Pd NPs-PDA@Fe_3O_4 and Pd NPs-PDA@UVM-7 shows that the PDA@Fe_3O_4 support presents an improved catalytic activity. This enhancement is likely originated by the different morphology of the Pd aggregates, which are smaller in size, but more dispersed on the magnetite core catalyst. Finally, it is worth noting that Pd NPs-PDA@Fe_3O_4 catalyst is quite active compared to other materials reported in the literature. For instance, the Pd NPs-Fe_3O_4@SiO_2 catalyst [62], a structurally close material, has a much lower $TOF_{1/2}$ (263 h^{-1}) than that reported in this work for the Pd NPs-PDA@Fe_3O_4 material.

3.3.2. Catalysts activity with regard nitrobenzene and 4-chloronitrobenzene

The activity of Pd NPs-PDA@Fe_3O_4 and Pd NPs-PDA@UVM-7 for reduction of $NO_2-C_6H_4-R$ (R = H,Cl) was checked in order to probe the usefulness of the synthesized materials. Unlike

4-nitrophenol, the reduction of nitroarenes normally proceeds though two consecutive steps involving the nitroso and hidroxylamino intermediate products [70, 88], as shows Fig. 7. This

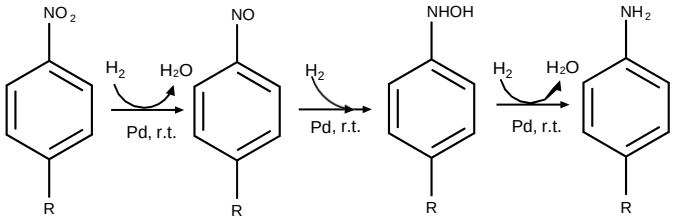

Figure 7: Non-condensative pathway for the Haber mechanism.

issue implies that the use of $TOF_{1/2}$ method introduced above could lead to misleading comparisons due to the relationship $x(t) = (A_t - A_\infty)/(A_0 - A_\infty)$ utilized for calculation of conversion is no longer valid.

The factorial multivariate-curve-resolution (MCR) methodology set out in section §2.6 constitutes an alternative to compare properly the catalytic activity. The MCR methodology belongs to the hard-modeling chemometric algorithms family [89], as it makes use of the rate law associated to a reaction mechanism to calculate the array **C** appearing in Eq. 6. In this line, array **C** was calculated by integration of the ordinary differential equation system (ODE) associated to the mechanism described by Eqs. 9-13, which has been reported in the literature [88],

$$BH_4^- + 4\,H_2O \longrightarrow B(OH)_4^- + 4\,H_2 \tag{9}$$

$$H_2 + 2\theta_L \underset{}{\overset{K_H}{\rightleftharpoons}} 2\theta_H \tag{10}$$

$$A_1 + \theta_L \underset{}{\overset{K_A}{\rightleftharpoons}} \theta_A \tag{11}$$

$$\theta_A + 2\theta_H \xrightarrow{k_1} A_2 + H_2O + 3\theta_L \tag{12}$$

$$4\theta_H + A_2 \xrightarrow{k^2} A_3 + H_2O + 4\theta_L \tag{13}$$

In the mechanism, A_1, A_2, and A_3 stand for nitroarene, nitrosoarene, and aminoarene species, θ_L represents the molar concentration of free catalytic centers, and θ_H and θ_A are the concentration of active centers occupied by hydrogen and 4-nitroarene derivatives.

The mechanism considers that BH_4^- reacts with the solvent (water and/or MeOH) generating H_2. Hereunder, hydrogen and the 4-nitroarene adsorb competitively onto the active Pd centers, in particular hydrogen does so in a dissociative manner. The adsorbed species react each other releasing the nitrosoarene to the medium, which reacts with hydrogen radicals on the catalyst yielding an aminoarene species. In dilute media, N-phenylhydroxylamine derivative was not observed as an intermediate product for both nitroarenes, thus the general scheme 7 simplified to the following formal mechanism,

$$NO_2\_C_6H_4\_R \xrightarrow[H_2,\,Pd]{\kappa^1} NO\_C_6H_4\_R \xrightarrow[H_2,\,Pd]{\kappa^2} NH_2-C_6H_4-R$$

where water molecules have been omitted for sake of simplicity. Considering that the Langmuir-Hinshelwood model applies to the kinetics of 4-nitroarene reduction [90], and the Rideal-Eley

model is fulfilled for reduction of the nitroso intermediate, the rate law in Eq.14 was deduced,

$$\frac{d\mathrm{C}}{dt} = \frac{d}{dt}\begin{pmatrix}[\mathrm{A}_1]\\ [\mathrm{A}_1]\\ [\mathrm{A}_2]\end{pmatrix} = \begin{bmatrix}-1 & 0\\ 1 & -1\\ 0 & 0\end{bmatrix}\begin{pmatrix}r_1\\ r_2\end{pmatrix} \qquad (14)$$

In Eq. 14, θ stands for the overall molar concentration of Pd, and the expression for the rates of the various steps (r_i) are given by Eqs. 15-16,

$$r_1 = k_1 \frac{K_A^{-1}(K_H[\mathrm{H}_2])^{1/2}\theta^2}{((1+(K_H[\mathrm{H}_2])^{\frac{1}{2}})K_A^{-1}+[\mathrm{A}_1])^2}[\mathrm{A}_1] = \frac{a_1[\mathrm{A}_1]}{(a_2+[\mathrm{A}_1])^2} \qquad (15)$$

$$r_2 = k_2 \frac{K_A^{-1}(K_H[\mathrm{H}_2])^{1/2}\theta^2}{(1+(K_H[\mathrm{H}_2])^{\frac{1}{2}})K_A^{-1}+[\mathrm{A}_1]}[\mathrm{A}_2] = \frac{a_3[\mathrm{A}_2]}{(a_2+[\mathrm{A}_1])^2} \qquad (16)$$

The a_i coefficients constitute a set of parameters that can be determined from least-squares regression (Table 2). It is observed that a_2 coefficient is small compared to $[\mathrm{A}_1]$. This circumstance would explain the initial zero-order behavior observed for the nitroarene decrease at the reaction beginning, (Figure 8d). Nevertheless, the small value of a_2 tends to correlate the remainder parameters making rate comparisons based on their absolute values unreliable. In order to solve these issues, Table 2 includes the ratios $\kappa_i = a_i/a_2$ defined by Eq. 17, that have a simpler chemical meaning,

$$\kappa_i = \frac{a_i}{a_2} = k_i\theta^n\frac{(K_H[\mathrm{H}_2])^{1/2}}{1+(K_H[\mathrm{H}_2])^{\frac{1}{2}}} \qquad (17)$$

Indeed, Eq. 17 simplifies under two limit assumptions. If $K_H[\mathrm{H}_2])^{1/2} << 1$, i.e. the effective concentration of hydrogen is low, then $\kappa_i = k_i\theta^n(K_H[\mathrm{H}_2])^{1/2}$. Alternatively, if $(K_H[\mathrm{H}_2])^{1/2}) >> 1$, i.e. there is a high availability of hydrogen in the medium, then the coefficient is interpreted as $\kappa_i = k_i\theta^n$. In any case, κ_i coefficients were proportional to the rate constants of the corresponding reduction steps in excess of hydrogen (kinetic runs were carried out 300-600:1, BH_4^-:$RC_6H_4NO_2$ mole ratio).

Table 2: Kinetic parameters calculated from the MCR analysis for the reaction $NO_2-C_6H_4-R \longrightarrow NH_2-C_6H_4-R$ catalyzed by Pd NPs-PDA@Fe_3O_4 and Pd NPs-PDA@UVM-7 in MeOH/H_2O 1:1 at room temperature.(R = H,Cl)

R	$a_1 \times 10^{11}$ /$s^{-1}M^2$	$a_2 \times 10^5$ /M	$a_3 \times 10^8$ /$s^{-1}M$	$^{\dagger}\kappa_1 \times 10^6$ /$s^{-1}M^{-1}$	$^{\dagger}\kappa_2 \times 10^3$ /s^{-1}	R	LOF
			Pd NPs-PDA@Fe_3O_4				
H	0.53	0.47	0.96	1.13	2.06	0.999_4	3.0
Cl	7.40	0.75	67.1	9.81	89.0	0.99_7	5.6
			Pd NPs-PDA@UVM-7				
H	9.37	2.07	10.4	4.53	5.05	0.999	3.7
Cl	31.3	6.31	44.6	4.95	7.07	0.999_7	2.2

† See Eq. 17.

Figures 8, S6, S7, S8, and Table 2 gathers the MCR results for both catalysts. To clarify the

methodology, Figure 8 shows the MCR results for nitrobenzene reduction catalyzed by Pd NPs-PDA@UVM-7. Figure 8a shows the initial data, i.e. the absorbance change with time. Figure

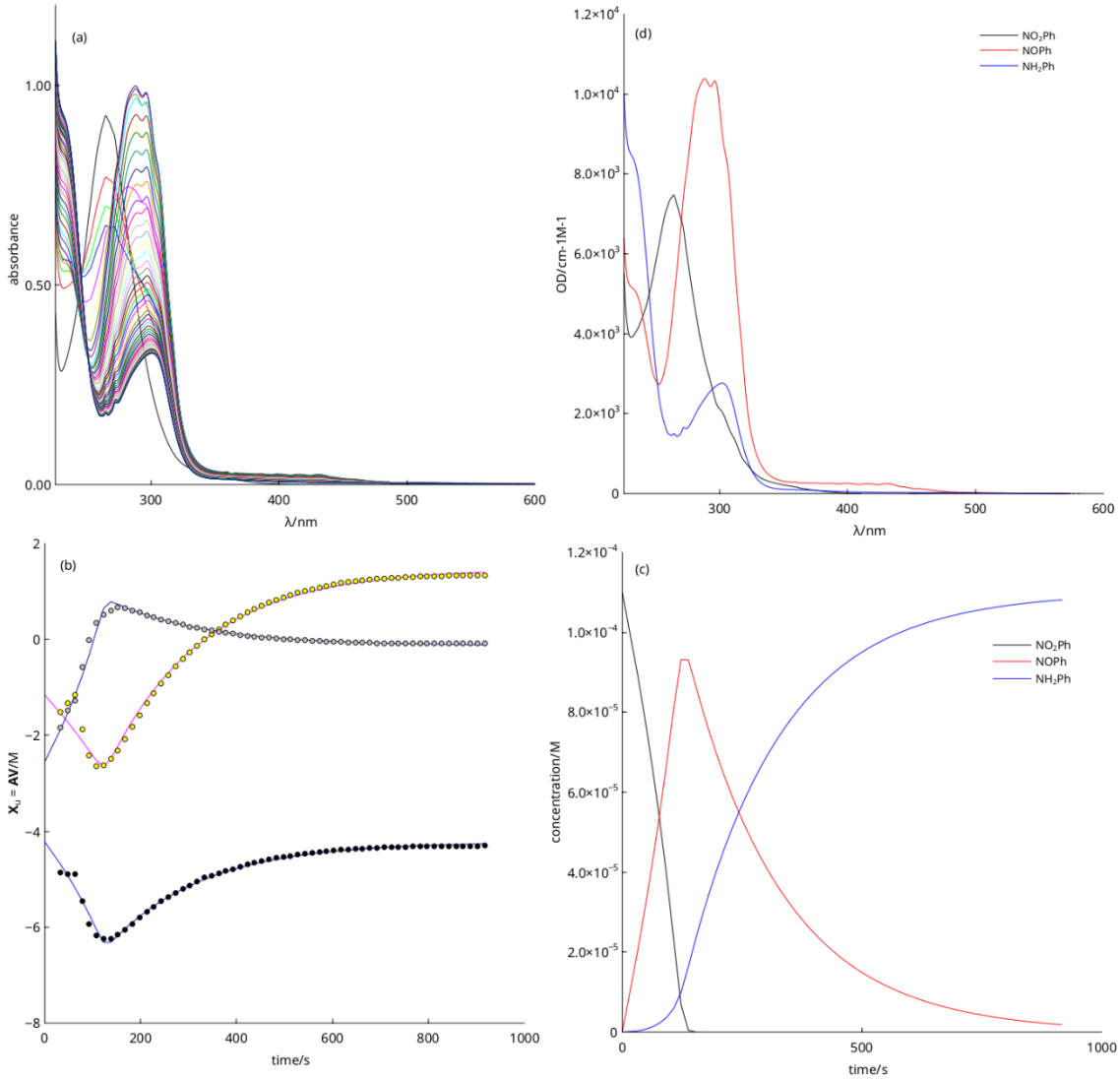

Figure 8: MCR analysis for reduction of nitrobenzene with $NaBH_4$ in MeOH/water 1:1 v/v at room temperature catalyzed by Pd NPs-PDA@UVM-7. (**a)** Evolution of absorbance (spectra taken every 15 s); (**b**) Abstract responses ($\mathbf{X}_u$ = **AV**) calculated from experimental data (circles); solid lines correspond to the non-linear regression of experimental abstract responses. (**c-d)** Evolution of composition and optical density spectra of nitrobenzene, nitrosobenzene and aniline calculated from MCR analysis of data shown in (a);

8b shows the MCR transformation of the experimental data into the so called abstract responses ($\mathbf{X}_u = \mathbf{AV}$). These quantities are precisely the ones that are fitted by least squares to obtain the a_i coefficients. In part (b) of the figure, symbols represent the experimental abstract responses, while the solid lines were calculated from the least-squares fitting to Eqs.14-16. Finally, Figures 8c and 8d show the concentration and the approximate optical density spectra profiles resulting from the MRC analysis. There is a good correlation ($R > 99$ in most cases) between experimental and calculated responses, the LOF index (lack of fit, i.e. that part of information that cannot be explained by the model) ranging between 2% to 5%. Both statistical indices support the model given by Eqs. 9-13 used for the activity comparison.

Values of κ_1 and κ_2 show that 4-chlorobenzene is reduced faster than nitrobenzene by both materials. For Pd NPs-PDA@Fe_3O_4 there is a clear relationship between the substituent electronegativity and the reduction rate. Pd NPs-PDA@UVM-7 follows the same trend, but the rate differences are not so significant. Unexpectedly, nitrobenzene was reduced faster by Pd NPs-PDA@UVM-7, suggesting that the catalyst morphology also plays a relevant role in the reaction kinetics.

As discussed, the main morphological differences in catalysts lie in the dispersion and size of the Pd domains, which are smaller and more dispersed for Pd NPs-PDA@Fe_3O_4, and the surface area and porosity, which are much more pronounced for Pd NPs-PDA@UVM-7. For Pd NPs-PDA@Fe_3O_4, the reaction likely takes place on the numerous Pd crystallites dispersed on the PDA surface, so the adsorption of the nitroarene has little influence on the reaction rate due to the active centers are fully accessible. In this case, the electronic factors (as electronegativity) determine the activity. For Pd NPs-PDA@UVM-7, the diffusion through the pore system, and the reduced accessibility of the Pd centers facilitate the nitrobenzene retention determining the catalytic activity. This effect compensates the substituent electronegativity, balancing the activity of the tested nitroarenes.

Figures 8c and S6d, S7d, and S8d show the concentration vs. time curves calculated from the MCR analysis. The plots show that reduction of functional groups $-NO_2$ to $-NO$, and $-NO$ to $-NH_2$ are well separated in time, producing a rapid reduction to $-NO$, which exhausts rapidly the $-NO_2$. This reaction is followed by a slower reduction of $-NO$ to $-NH_2$, which constitutes the rate limiting step.

4. Conclusions

With a simple synthesis method we have anchored in two stages Pd NPs on two inorganic supports, silica and magnetite, covered with PDA. The resulting materials are active for green and sustainable catalytic reduction of nitroarenes: only small amounts of expensive noble-metal are required, no toxic and/or hazardous reagents are used in the synthesis, or under the working catalytic conditions that occur under mild conditions, and without tedious work-up process.

Simple procedural parameters such as the washing extent or the separation method (through centrifugation or magnetically) allows us to control the Pd amount together with its distribution and aggregation level of the primary Pd NPs (the catalytic sites). Furthermore, we show how the final morphology of the catalyst (with greater or lesser porous character) has an important effect on its activity. Morphology can be controlled by selection of the inorganic skeleton (porous or massive; with aggregated or isolated particles). From our results, it could be anticipated that when porous or organized cores are used in the form of clusters (as occurs for UVM-7 silica), the final morphology after coating with PDA is reminiscent of that of the starting inorganic core, however, when skeletons based on isolated or slightly aggregated nanoparticles are selected,

the final morphology is less dependent on the inorganic core and more closely resembles PDA globules containing trapped oxidic particles. In any case, the selection of the particle sizes and its relationship with the amount of PDA allows providing the final composite of a certain textural porosity.

The $TOF_{1/2}$ analysis suggest that Pd NPs anchored on PDA@Fe_3O_4 present higher catalytic activity for reduction 4-nitrophenol than those fixed on PDA@UVM-7. The estimated $TOF_{1/2c}$ value (7.5×10^4 $h^{-1}M^{-1}$) is much higher than that of other catalysts based on SiO_2, magnetite, or mixed magnetite/SiO_2 cores. Moreover, Pd NPs present an activity according to their palladium load for the PDA@UVM-7 material. The difference in activity of both supports is related to their morphology. The silica core is less active due to the porosity of the material, together with the larger size of the Pd crystallites, reduce the number of active centers making them less accessible for the catalytic process.

The TOF-based methodology cannot be used for multi-step reactions. In this case the multivariate curve analysis resolution (MCR) provides a semi-quantitative view of the processes occurring in the reactor, from which more reliable criteria for comparison of catalytic activity can be established. The catalysts have proven to be active against nitrobenzene and 4-chloronitrobenzene. The MCR analysis of the absorbance data indicates that the reduction proceeds through two steps well separated in time, namely the reduction of the nitro group to nitroso, and the latter to amino group. The analysis indicates that the first reduction constitutes the rate limiting step of the reaction. From the analysis, it is also evident that the reaction rate is influenced by both electronic factors and morphology of support. For the magnetic core catalyst, the electronic factors (i.e. electronegativity) are the most important, and a very rapid reduction of the chlorinated nitroarene is observed. For the silica core catalyst, morphology (i.e. porosity and crystallite size) predominates, with electronic factors being attenuated in favor of other processes such as the intra-pore diffusion of the substrates. In this case, similar reaction rates are observed for both substrates. The results show that the Pd NP catalysts supported on PDA are a good option to perform a fast, quantitative reduction of nitroarenes.

Supplementary information

- Figure S1: TGA results for Pd NPs-PDA@UVM-7 and Pd NPs-PDA@Fe_3O_4.
- Figure S2: STEM-mapping of Pd NPs-@PDAFe_3O_4 material.
- Figure S3: N_2 adsorption-desorption isotherms of Pd NPs-PDA@UVM-7 and Pd NPs-PDA@Fe_3O_4 catalysts.
- Figure S4: XPS spectrum of Pd NPs-PDA@Fe_3O_4 catalyst.
- Figure S5: UV-vis data for $NO_2-C_6H_4OH \longrightarrow NH_2-C_6H_4OH$ catalyzed by Pd NPs-PDA@UVM-7.
- Figure S6: MCR analysis results for $NO_2-C_6H_5 \longrightarrow NH_2-C_6H_5$ catalyzed by Pd NPs-PDA@Fe_3O_4.
- Figure S7: MCR analysis results for $NO_2-C_6H_4Cl \longrightarrow NH_2-C_6H_4Cl$ catalyzed by Pd NPs-PDA@Fe_3O_4.
- Figure S8: MCR analysis results for $NO_2-C_6H_4Cl \longrightarrow NH_2-C_6H_4Cl$ catalyzed by Pd NPs-PDA@UVM-7.

Acknowledgments

We appreciate the technical support of the SCSIE of the Universitat de Valencia and Electron Microscopy Service of the Universidad Politécnica de Valencia, the Ministerio de Ciencia, Innovación y Universidades and FEDER Spain, grant number RTI2018-100910-B-C44 for funding this research.

References

[1] L. R. Shultz, L. Hu, K. Preradovic, M. J. Beazley, X. Feng, T. Jurca, ChemCatChem 11 (2019) 2590–2595. doi:10.1002/cctc.201900260.
[2] Hasan, Shehadi, Al-Bab, Elgamouz, Catalysts 9 (2019) 839. doi:10.3390/catal9100839.
[3] J. Xia, G. He, L. Zhang, X. Sun, X. Wang, Appl. Catal., B 180 (2016) 408–415. doi:10.1016/j.apcatb.2015.06.043.
[4] S. Yu, J. Hu, J. Wang, Journal of Hazardous Materials 177 (2010) 1061–1067. doi:10.1016/j.jhazmat.2010.01.028.
[5] M. Venkatesham, D. Ayodhya, A. Madhusudhan, N. V. Babu, G. Veerabhadram, Applied Nanoscience 4 (2012) 113–119. doi:10.1007/s13204-012-0180-y.
[6] A. Corma, P. Serna, Science 313 (2006) 332–334. doi:10.1126/science.1128383.
[7] T. Aditya, A. Pal, T. Pal, Chem. Commun. 51 (2015) 9410–9431. doi:10.1039/C5CC01131K.
[8] L. Ai, J. Jiang, Bioresour. Technol. 132 (2013) 374–377. doi:10.1016/j.biortech.2012.10.161.
[9] C. Hou, D. Zhao, W. Chen, H. Li, S. Zhang, C. Liang, Nanomaterials 10 (2020) 426. doi:10.3390/nano10030426.
[10] P. Pachfule, S. Kandambeth, D. D. D´ıaz, R. Banerjee, Chem. Commun. 50 (2014) 3169–3172. doi:10.1039/c3cc49176e.
[11] J. C. Spain, Annu. Rev. Microbiol. 49 (1995) 523–555. doi:10.1146/annurev.mi.49.100195.002515.
[12] Y. Y. Liu, Y. H. Zhao, Y. Zhou, X. L. Guo, Z. T. Chen, W. J. Zhang, Y. Zhang, J. Chen, Z. M. Wang, L. T. Sun, T. Zhang, Nanotechnology 29 (2018) 315702. doi:10.1088/1361-6528/aac3e8.
[13] K. Bhaduri, B. D. Das, R. Kumar, S. Mondal, S. Chatterjee, S. Shah, J. J. Bravo-Suárez, B. Chowdhury, ACS Omega 4 (2019) 4071–4081. doi:10.1021/acsomega.8b03655.
[14] Y.-C. Chang, D.-H. Chen, Journal of Hazardous Materials 165 (2009) 664–669. doi:10.1016/j.jhazmat.2008.10.034.
[15] T.-L. Lai, K.-F. Yong, J.-W. Yu, J.-H. Chen, Y.-Y. Shu, C.-B. Wang, Journal of Hazardous Materials 185 (2011) 366–372. doi:10.1016/j.jhazmat.2010.09.044.
[16] J. Li, D. Kuang, Y. Feng, F. Zhang, Z. Xu, M. Liu, Journal of Hazardous Materials 201-202 (2012) 250–259. doi:10.1016/j.jhazmat.2011.11.076.
[17] J.-R. Chiou, B.-H. Lai, K.-C. Hsu, D.-H. Chen, Journal of Hazardous Materials 248-249 (2013) 394–400. doi:10.1016/j.jhazmat.2013.01.030.
[18] H. K. Kadam, S. G. Tilve, RSC Adv. 5 (2015) 83391–83407. doi:10.1039/c5ra10076c.
[19] P. Lara, K. Philippot, Catal. Sci. Technol. 4 (2014) 2445–2465. doi:10.1039/C4CY00111G.
[20] D. Formenti, F. Ferretti, F. K. Scharnagl, M. Beller, Chem. Rev. 119 (2019) 2611–2680. doi:10.1021/acs.chemrev.8b00547.
[21] S. Doherty, J. G. Knight, T. Backhouse, A. Bradford, F. Saunders, R. A. Bourne, T. W. Chamberlain, R. Stones, A. Clayton, K. Lovelock, Catal. Sci. Technol. 8 (2018) 1454–1467. doi:10.1039/C7CY02557B.
[22] S. Doherty, J. G. Knight, T. Backhouse, R. J. Summers, E. Abood, W. Simpson, W. Paget, R. A. Bourne, T. W. Chamberlain, R. Stones, K. R. J. Lovelock, J. M. Seymour, M. A. Isaacs, C. Hardacre, H. Daly, N. H. Rees, ACS Catalysis 9 (2019) 4777–4791. doi:10.1021/acscatal.9b00347.
[23] M. Orlandi, D. Brenna, R. Harms, S. Jost, M. Benaglia, Org. Process Res. Dev. 22 (2018) 430–445. doi:10.1021/acs.oprd.6b00205.
[24] P. Zhao, X. Feng, D. Huang, G. Yang, D. Astruc, Coord. Chem. Rev. 287 (2015) 114 – 136. doi:https://doi.org/10.1016/j.ccr.2015.01.002.
[25] P. Serna, A. Corma, ACS Catalysis 5 (2015) 7114–7121. doi:10.1021/acscatal.5b01846.
[26] E. H. Boymans, P. T. Witte, D. Vogt, Catalysis Science & Technology 5 (2015) 176–183. doi:10.1039/c4cy00790e.
[27] Y. Shi, L. Liu, F. Zhang, M. Niu, Y. Zhao, Y. Fan, Y. Liang, M. Liu, Z. Zhang, J. Wang, Polymers 9 (2017). doi:10.3390/polym9090459.
[28] S. Chen, L.-L. Ling, S.-F. Jiang, H. Jiang, Green Chemistry 22 (2020) 5730–5741. doi:10.1039/d0gc01835j.
[29] Z. Yan, L. Fu, X. Zuo, H. Yang, Appl. Catal., B 226 (2018) 23–30. doi:10.1016/j.apcatb.2017.12.040.
[30] G. Wang, F. Li, L. Li, J. Zhao, X. Ruan, W. Ding, J. Cai, A. Lu, Y. Pei, ACS Omega 5 (2020) 8839–8846. doi:10.1021/acsomega.0c00437.

[31] M. M. Trandafir, A. Moragues, P. Amorós, V. I. Parvulescu, Catal. Today 355 (2020) 893–902. doi:10.1016/j.cattod.2019.02.053.
[32] M. Zhang, G. Li, X. Sun, Y. Jiang, X. Zhang, J. Mater. Chem. A 5 (2017) 20789–20796. doi:10.1039/C7TA06204D.
[33] Y. Liu, G. Li, R. Qin, D. Chen, Langmuir 32 (2016) 13675–13686. doi:10.1021/acs.langmuir.6b03340.
[34] H. Lee, S. M. Dellatore, W. M. Miller, P. B. Messersmith, Science 318 (2007) 426–430. doi:10.1126/science.1147241.
[35] H. Lee, J. Rho, P. B. Messersmith, Adv. Mater. 21 (2009) 431–434. doi:10.1002/adma.200801222.
[36] J. H. Ryu, P. B. Messersmith, H. Lee, ACS Appl. Mater. Interfaces 10 (2018) 7523–7540. doi:10.1021/acsami.7b19865.
[37] Y. Liu, K. Ai, L. Lu, Chem. Rev. 114 (2014) 5057–5115. doi:10.1021/cr400407a.
[38] R. Liu, Y. Guo, G. Odusote, F. Qu, R. D. Priestley, ACS Appl. Mater. Interfaces 5 (2013) 9167–9171. doi:10.1021/am402585y.
[39] E. K. Jeon, E. Seo, E. Lee, W. Lee, M.-K. Um, B.-S. Kim, Chem. Commun. 49 (2013) 3392. doi:10.1039/c3cc00115f.
[40] H. Huang, Z. He, X. Lin, W. Ruan, Y. Liu, Z. Yang, Appl. Catal., A 490 (2015) 65–70. doi:10.1016/j.apcata.2014.11.014.
[41] Y. Yang, A. C. Reber, S. E. Gilliland, C. E. Castano, B. F. Gupton, S. N. Khanna, J. Catal. 360 (2018) 20–26. doi:10.1016/j.jcat.2018.01.027.
[42] M. A. Hussain, M. Yang, T. J. Lee, J. W. Kim, B. G. Choi, J. Colloid Interface Sci. 451 (2015) 216 – 220. doi:10.1016/j.jcis.2015.03.062.
[43] J.-X. Ma, H. Yang, S. Li, R. Ren, J. Li, X. Zhang, J. Ma, RSC Adv. 5 (2015) 97520–97527. doi:10.1039/c5ra13361k.
[44] W. Ye, J. Yu, Y. Zhou, D. Gao, D. Wang, C. Wang, D. Xue, Appl. Catal., B 181 (2016) 371–378. doi:10.1016/j.apcatb.2015.08.013.
[45] F. Ren, C. Zhai, M. Zhu, C. Wang, H. Wang, D. Bin, J. Guo, P. Yang, Y. Du, Electrochim. Acta 153 (2015) 175–183. doi:10.1016/j.electacta.2014.11.184.
[46] J. Zhou, B. Duan, Z. Fang, J. Song, C. Wang, P. B. Messersmith, H. Duan, Adv. Mater. 26 (2014) 701–705. doi:10.1002/adma.201303032.
[47] S. Sadjadi, G. Lazzara, M. Malmir, M. M. Heravi, J. Catal. 366 (2018) 245–257. doi:10.1016/j.jcat.2018.08.013.
[48] S. K. Movahed, N. F. Lehi, M. Dabiri, J. Catal. 364 (2018) 69–79. doi:10.1016/j.jcat.2018.05.003.
[49] A. Kunfi, Z. May, P. Németh, G. London, J. Catal. 361 (2018) 84–93. doi:10.1016/j.jcat.2018.02.031.
[50] H. Veisi, A. Nikseresht, S. Mohammadi, S. Hemmati, Chin. J. Catal. 39 (2018) 1044–1050. doi:10.1016/S1872-2067(18)63049-9.
[51] Y. Song, H. Jiang, B. Wang, Y. Kong, J. Chen, ACS Appl. Mater. Interfaces 10 (2018) 1792–1801. doi:10.1021/acsami.7b18136.
[52] J. Manna, S. Akbayrak, S. Özkar, Appl. Catal., B 208 (2017) 104–115. doi:10.1016/j.apcatb.2017.02.037.
[53] M. Ródenas, J. E. Haskouri, J. V. Ros-Lis, M. D. Marcos, P. Amorós, M. Á. Úbeda, F. Pérez-Pla, Catalysts 10 (2020) 449. doi:10.3390/catal10040449.
[54] P. Alfonso Albiñana, J. El Haskouri, M. D. Marcos, F. Estevan, P. Amorós, M. A. Úbeda, F. Pérez-Pla, J. Catal. 367 (2018) 283–295. doi:10.1016/j.jcat.2018.09.014.
[55] C. Su, Journal of Hazardous Materials 322 (2017) 48–84. doi:10.1016/j.jhazmat.2016.06.060.
[56] M. Li, X. Zhou, J. Sun, H. Fu, X. Qu, Z. Xu, S. Zheng, Science of The Total Environment 663 (2019) 673–685. doi:10.1016/j.scitotenv.2019.01.392.
[57] A. V. Dubey, A. V. Kumar, RSC Adv. 6 (2016) 46864–46870. doi:10.1039/c6ra03395d.
[58] J. Manna, S. Akbayrak, S. Özkar, RSC Advances 6 (2016) 102035–102042. doi:10.1039/c6ra23007e.
[59] A. Kunfi, V. Szabó, Á. Mastalir, I. Bucsi, M. Mohai, P. Németh, I. Bertóti, G. London, ChemCatChem 9 (2017) 3236–3244. doi:10.1002/cctc.201700609.
[60] H. Guo, R. Zheng, H. Jiang, Z. Xu, A. Xia, BMC Chemistry 13 (2019). doi:10.1186/s13065-019-0649-9.
[61] H. Guo, R. Zheng, H. Jiang, Z. Xu, A. Xia, Molecules 24 (2019) 1730. doi:10.3390/molecules24091730.
[62] E. Farzad, H. Veisi, J. Ind. Eng. Chem. 60 (2018) 114–124. doi:10.1016/j.jiec.2017.10.017.
[63] H. Veisi, T. Tamoradi, A. Rashtiani, S. Hemmati, B. Karmakar, J. Ind. Eng. Chem. 90 (2020) 379–388. doi:10.1016/j.jiec.2020.06.030.
[64] J. Yang, Y. Zhu, M. Fan, X. Sun, W. D. Wang, Z. Dong, Journal of Colloid and Interface Science 554 (2019) 157–165. doi:10.1016/j.jcis.2019.07.006.
[65] R. Ma, P. Yang, Y. Ma, F. Bian, ChemCatChem 10 (2018) 1446–1454. doi:10.1002/cctc.201701693.
[66] S. Wunder, Y. Lu, M. Albrecht, M. Ballauff, ACS Catal. 1 (2011) 908–916. doi:10.1021/cs200208a.
[67] S. Gu, S. Wunder, Y. Lu, M. Ballauff, R. Fenger, K. Rademann, B. Jaquet, A. Zaccone, J. Phys. Chem. C 118 (2014) 18618–18625. doi:10.1021/jp5060606.
[68] N. E. Larm, N. Bhawawet, J. A. Thon, G. A. Baker, New J. Chem. 43 (2019) 17932–17936.

doi:10.1039/c9nj01745c.
[69] F. Haber, Electrochem.Angew. Phys. Chem. (1898).
[70] A. Corma, P. Concepción, P. Serna, Angew. Chem. Int. Ed. 46 (2007) 7133–7133. doi:10.1002/anie.200790188.
[71] E. Bezemer, S. C. Rutan, Chemom. Intell. Lab. Syst. 59 (2001) 19–31. doi:10.1016/s0169-7439(01)00141-1.
[72] S. Bijlsma, A. K. Smilde, Anal. Chim. Acta 396 (1999) 231 – 240. doi:10.1016/S0003-2670(99)00442-0.
[73] M. Maeder, Y. M. Neuhold, Taylor and Francis, Boca Raton, 2006.
[74] J. El Haskouri, J. M. Morales, D. de Zárate, L. Fernández, J. Latorre, C. Guillem, A. Beltrán, D. Beltrán, P. Amorós, Inorg. Chem. 47 (2008) 8267–8277. doi:10.1021/ic800893a.
[75] E. P. Barrett, L. G. Joyner, P. P. Halenda, Journal of the American Chemical Society 73 (1951) 373–380. doi:10.1021/ja01145a126.
[76] J. Landers, G. Y. Gor, A. V. Neimark, Colloids Surf., A 437 (2013) 3–32. doi:10.1016/j.colsurfa.2013.01.007.
[77] E. R. Malinowski, Factor Analysis in Chemistry, 2 ed., Wiley Interscience, N. York, 1991.
[78] H. Gampp, M. Maeder, C. J. Meyer, A. D. Zuberbühler, Talanta 32 (1985) 1133–1139. doi:10.1016/0039-9140(85)80238-1.
[79] E. R. Malinowski, Anal. Chem. 49 (1977) 612–617. doi:10.1021/ac50012a027.
[80] E. A. Sylvestre, W. H. Lawton, M. S. Maggio, Technometrics 16 (1974) 353–368. doi:10.1080/00401706.1974.10489204.
[81] R. Bonneau, J. Wirz, A. D. Zuberbuhler, Pure Appl. Chem. 69 (1997) 979–992. doi:10.1351/pac199769050979.
[82] W. H. Lawton, E. A. Sylvestre, Technometrics 13 (1971) 617–633. doi:10.1080/00401706.1971.10488823.
[83] J. Bezanson, S. Karpinski, V. B. Shah, A. Edelman, CoRR abs/1209.5 (2012).
[84] J. A. Nelder, R. Mead, The Computer Journal 7 (1965) 308–313. doi:10.1093/comjnl/7.4.308.
[85] S. G. Johnson, The NLOPT nonlinear-optimization package, http://ab-initio.mit.edu/nlopt, 2012.
[86] C. W. Gear, L. R. Petzold, SIAM J. Numer. Anal. 21 (1984) 716–728. URL: http://www.jstor.org/stable/2157004.
[87] C. Rackauckas, Q. Nie, Journal of Open Research Software 5 (2017) 10. doi:10.5334/jors.151.
[88] E. A. Gelder, S. D. Jackson, C. M. Lok, Chem. Commun. (2005) 522–524. doi:10.1039/B411603H.
[89] F. F. P. Pla, J. B. Baeza, E. Llopis, M. P. Baeza, L. Fernández, International Journal of Chemical Kinetics 48 (2016) 449–463. doi:10.1002/kin.21004.
[90] K. V. Kumar, K. Porkodi, F. Rocha, Catal. Commun. 9 (2008) 82 – 84. doi:10.1016/j.catcom.2007.05.019.